g-C$_3$N$_4$/Nb$_2$O$_5$ heterostructures tailored by sonochemical synthesis: Enhanced photocatalytic performance in oxidation of emerging pollutants driven by visible radiation

Gelson T.S.T. da Silva [a,b], Kele T.G. Carvalho [b], Osmando F. Lopes [b,c], Caue Ribeiro [b,*]

[a] Departamento de Química, Universidade Federal de São Carlos – UFSCar, Rodovia Washington Luiz, km 235, CEP 13.565-905, São Carlos, SP, Brazil
[b] Laboratório Nacional de Nanotecnologia para o Agronegócio (LNNA) – Embrapa Instrumentação, Rua XV de Novembro, n° 1452, CEP 13.561-206, São Carlos, SP, Brazil
[c] Instituto de Química de São Carlos, Universidade de São Paulo – USP, Av. Trabalhador São Carlense, n° 400, CEP 13560-970, São Carlos, SP, Brazil

ABSTRACT

In this study, g-C$_3$N$_4$/Nb$_2$O$_5$ heterostructures were successfully prepared by a sonochemical method based on surface charge-induced heteroaggregation. Under visible irradiation, the heterostructured g-C$_3$N$_4$/Nb$_2$O$_5$ samples exhibited higher activity in the photooxidation of the drug amiloride (AML) and rhodamine B dye (RhB), compared to the pure g-C$_3$N$_4$ and Nb$_2$O$_5$ phases. The enhanced photocatalytic activity of the heterostructures could be attributed to the effective formation of heterojunctions between the g-C$_3$N$_4$ and Nb$_2$O$_5$ semiconductors, causing the migration of photogenerated electrons and holes, hence increasing their lifetimes. Formation of the type-II heterostructure was confirmed by time-resolved photoluminescence, in which the 3CN:1Nb heterostructure showed the longest electron/hole pair lifetime. The 3CN:1Nb and 1CN:3Nb heterostructures exhibited high stability even after four cycles of reuse in RhB dye and drug AML oxidation, respectively. In summary, the combination of g-C$_3$N$_4$ with Nb$_2$O$_5$ to produce a type-II heterostructure is a good strategy to overcome important challenges in photocatalysis.

© 2017 Elsevier B.V. All rights reserved.

1. Introduction

The presence of organic contaminants such as pesticides, pharmaceuticals, and dyes in rivers and lakes, even at low concentrations, can seriously affect human health and the environment. Amiloride, a drug extensively used for the treatment of hypertension, belongs to a class of pharmaceutical compounds that are often found in wastewater and can adversely affect water quality [1–3]. Rhodamine B, a dye used in the textile industry, is another organic pollutant found in wastewater that can be prejudicial to the environment and human health because of its resistance to biodegradation and its potential carcinogenicity [4,5]. There is therefore a need for the development of efficient treatment technologies for the removal of these compounds from wastewater. Advanced oxidation processes (AOPs) such as heterogeneous photocatalysis have attracted great interest for this purpose, especially using semiconductors that can be activated under visible irradia-tion. Graphitic carbon nitride (g-C$_3$N$_4$) has been identified as a useful organic semiconductor that can be easily obtained by poly-merization involving the thermal condensation of nitrogen-rich precursors such as cyanamide, urea, and melamine [6–8]. Much of the interest in the use of this material is due to its low band gap value (E$_g$ ~2.7 eV) and suitable band structure to drive reactions involving reduction (such as artificial photosynthesis and water splitting) or oxidation (such as degradation of organic pollutants) [9,10].

However, bulk g-C$_3$N$_4$ exhibits a low surface area and fast recombination of photogenerated electron/hole pairs, which reduce its photocatalytic activity [11]. Strategies such as morphol-ogy control, exfoliation, non-metal doping, and deposition of metal nanoparticles have been proposed in order to improve its effi-ciency in photocatalytic processes [12–15]. An effective way to increase the photoactivity is to couple g-C$_3$N$_4$ with another semi-conductor by means of type-II heterojunctions [16]. In this type of heterojunction, the potential of the conduction and valence bands of a semiconductor is lower than that of the other semi-conductor [16,17], and promotes photogenerated charge transfer between the semiconductors, longer photogenerated electron/hole pair lifetimes, and a consequent enhancement of photocatalytic

properties [18–21]. Among various semiconductors, niobium oxide (Nb_2O_5) is a promising material for coupling to g-C_3N_4. Nb_2O_5 is an n-type semiconductor with an optical band gap of ~3.2 eV, high specific surface area, high surface acidity, and good photoactivity towards the degradation of organic pollutants [22–24]. Nb_2O_5 powder has been incorporated in many composites, such as Nb_2O_5/ZnO [22], TiO_2/Nb_2O_5 [25], Nb_2O_5/CuO [26], Nb_2O_5/RGO [27], and Nb_2O_5/iron oxide [28], resulting in significant increases in photocatalytic performance. However, until now there have been only two studies devoted to evaluating the photoactivity of heterostructures formed by g-C_3N_4 and Nb_2O_5 [29,30]. Major drawbacks of the systems described previously are long synthesis times and lack of control of heterostructure formation, which can lead to poor dispersion of Nb_2O_5 particles on the g-C_3N_4 surface, as well as a large particle size, hence decreasing the activity of the photocatalysts. Therefore, the synthesis route employed to produce suitable heterostructures based on g-C_3N_4 still remains a matter of study.

The sonochemical technique offers an interesting alternative means of obtaining heterostructures of g-C_3N_4 and Nb_2O_5. This method is simple, fast, and enables highly accurate control of synthesis parameters including time, energy input, and pH. Furthermore, the application of ultrasonic irradiation induces particle deagglomeration, which increases the surface area of the materials [31–33]. The sonochemical method enables use of a surface charge-induced heteroaggregation strategy, based on the dispersion of particles by physical methods and adjustment of the pH of the medium to a value between the points of zero charge (PZC) of the materials. This maximizes the electrostatic attraction between them, favoring the effective formation of heterojunctions and control of the morphology [15,34]. However, few studies have explored this strategy for photocatalysis and, to the best of our knowledge, there are no published papers concerning heterojunction formation in a semiconductor:g-C_3N_4 system.

Therefore, the purpose of this work was to synthesize a series of g-C_3N_4/Nb_2O_5 heterostructures by a sonochemical method based on surface charge-induced heteroaggregation, and to evaluate their photocatalytic activity in the degradation of rhodamine B (RhB) dye and the drug amiloride (AML), under visible irradiation. The charge
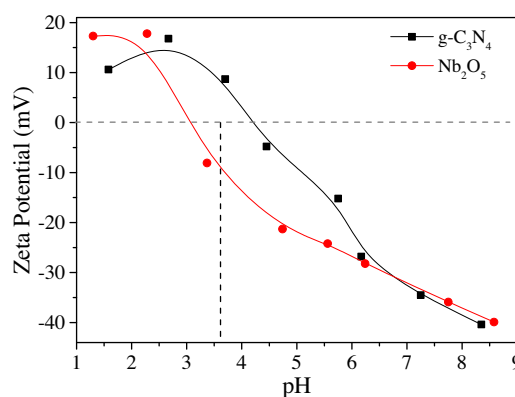

Fig. 1. Zeta potentials of g-C_3N_4 and Nb_2O_5, as a function of pH. The symbols correspond to the experimental data. The lines are provided to assist visual interpretation.

carrier dynamics was studied by time-resolved photoluminescence. Evaluation was also made of the pollutant photooxidation mechanism and the stability of the g-C_3N_4/Nb_2O_5 heterostructures.

2. Experimental

2.1. Preparation of the g-C_3N_4/Nb_2O_5 heterostructures

The g-C_3N_4 material was prepared by the thermal polymerization of urea (CH_4N_2O, Synth) in a muffle furnace under an air atmosphere from adapted method [35,36]. In a typical procedure, 10 g of urea powder was placed in a partially covered alumina crucible and heated at 550 °C for 2 h, using a heating rate of 3 °C min^{-1}, resulting in a yellow powder. Nb_2O_5 powder was synthesized using the peroxide oxidant method [23]. This consisted of dissolving 2 g of ammonium niobium oxalate ($NH_4[NbO(C_2O_4)_2(H_2O)_2] \cdot nH_2O$), supplied by CBMM (Brazil) and used as the Nb precursor, in 100 mL of deionized water and 4 mL of hydrogen peroxide (H_2O_2), followed by hydrothermal annealing at 120 °C for 12 h, as described elsewhere [23].
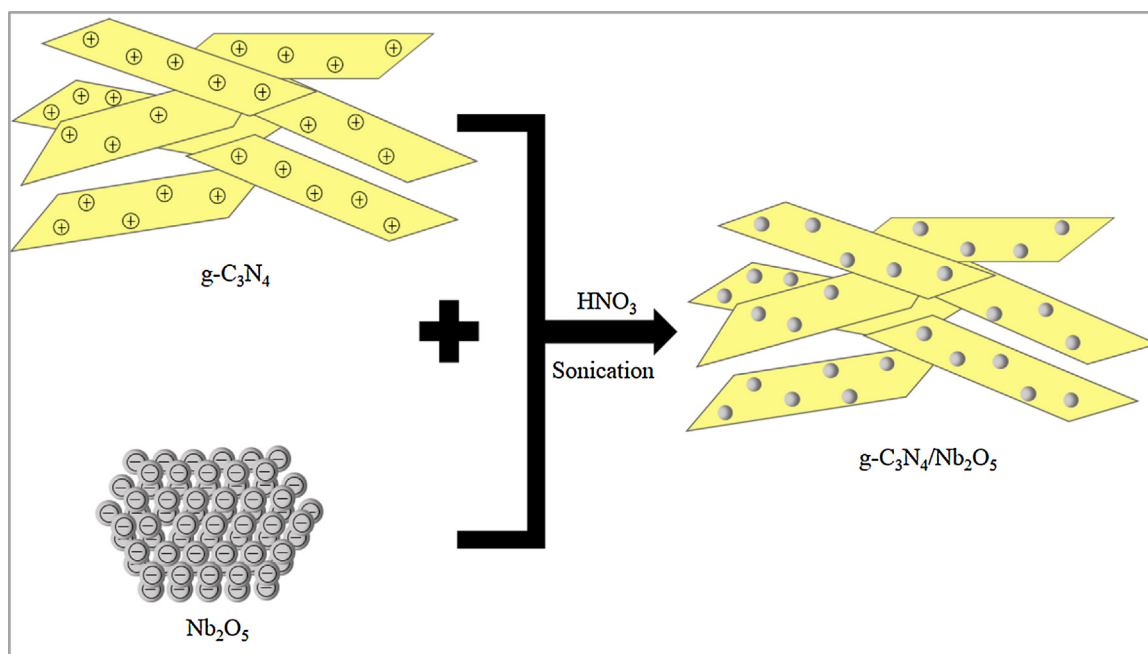
Scheme 1. Schematic illustration of the preparation process of the g-C_3N_4/Nb_2O_5 heterostructures.

The g-C_3N_4/Nb_2O_5 heterostructures were prepared using the surface charge-induced heteroaggregation method [34], in which opposite surface charges are the driving force (by electrostatic interaction) for the formation of heterojunctions between the g-C_3N_4 and Nb_2O_5 phases. As shown in Fig. 1, there is a pH range near pH 3.6 where g-C_3N_4 has a positive surface charge, due to the incomplete condensation of amino groups [37], while Nb_2O_5 has a negative surface charge, due to the presence of surface hydroxyl groups. Scheme 1 illustrates the preparation process used for the heterostructured samples. Typically, different amounts of the as-synthesized powders (g-C_3N_4 and Nb_2O_5) were placed in a beaker containing 130 mL of deionized water. Nitric acid (0.5 mol L^{-1}) was then added to the suspension, under continuous stirring, in order to adjust the pH to 3.6, followed by ultrasonic agitation for 2 h in an ice bath. The material obtained was washed with distilled water until reaching neutral pH, centrifuged, and dried at 50 °C overnight. The weight ratios between g-C_3N_4 and Nb_2O_5 used in the syntheses were 1:3, 1:1, and 3:1, which were labeled as 1CN:3Nb, 1CN:1Nb, and 3CN:1Nb, respectively. It was determined by thermogravimetric analysis (Fig. S1) that g-C_3N_4 contents in the CN:Nb heterostructures were approximately 37.6, 55.2, and 62.0 wt% for 1CN:3Nb, 1CN:1Nb, and 3CN:1Nb, respectively.

The efficiency of the proposed method for obtaining heterojunctions was confirmed by preparing a physical mixture of the g-C_3N_4 and Nb_2O_5 phases by simple grinding in an agate mortar, as well as by using an ultrasonic method similar to that described above, but at neutral pH (without any pH adjustment). These materials were obtained using a CN:Nb weight ratio of 3:1 and were labeled as 3CN:1Nb-PM and 3CN:1Nb-H_2O, respectively. The photocatalytic performances of these two samples were compared to that of the 3CN:1Nb heterostructure (Fig. S2).

2.2. Characterization of the materials

The materials were characterized by X-ray diffraction (XRD) using a Shimadzu XRD 600 diffractometer with nickel-filtered Cu Kα radiation, at 2θ from 5 to 70°, in continuous scan mode with a step width of 0.02° and a scan speed of 2° min^{-1}. Fourier transform infrared (FTIR) spectra were recorded from 4000 to 500 cm^{-1}, at a resolution of 4 cm^{-1}, using a Bruker Vertex 70 spectrophotometer. The morphologies of the samples were observed with a JEOL JSM-6701F field emission gun scanning electron microscope (FEG-SEM). The materials were also characterized by transmission electron microscopy (TEM), using an FEI Tecnai G2 F20 microscope operated at 200 kV. The TEM samples were prepared by wetting copper grids coated with formvar/carbon or ultrathin holey carbon film with drops of alcoholic suspensions, followed by drying in a desiccator. Diffuse reflectance spectrometry (DRS) spectra were recorded with a UV–vis spectrophotometer (UV-2700, Shimadzu) in the range from 200 to 800 nm. Magnesium oxide (MgO) pow-der was used as a reflectance standard. The zeta potential was measured at room temperature using a Zetasizer Nano-ZS analyzer (Malvern Instruments, UK), with the pH adjusted by dropwise addition of dilute HCl or NaOH solutions. The specific surface area (SSA) values were calculated according to the Brunauer-Emmett-Teller (BET) method, using N_2 adsorption data obtained at −196 °C using a Micromeritics ASAP-2020 system. Surface chemical analyses were performed with a K-Alpha XPS instrument (Thermo Fisher Scientific, UK), using Al Kα X-rays, >10^{-8} mbar of vacuum, and charge compensation during the measurements. A resolution of 1 eV, with 5 scans, was used for survey spectra, while high-resolution spectra were recorded at a resolution of 0.1 eV, with 50 scans. The binding energy was referenced to the C 1s peak at 284.7 eV. Data analysis was performed using CasaXPS software. The fluorescence lifetime was measured using a FluoTime 300 time-correlated single photon counting (TCSPC) instrument (PicoQuant, Germany) equipped with a picosecond-pulsed laser diode (LDH-P-C-405, 409 nm). The lifetime was measured at an emission wavelength of 535 nm. Thermogravimetric analyses (TGA) were performed on a Shimadzu TGA-50 equipment using oxidative atmosphere conditions (air flow rate of 60 mL min^{-1}), temperature range from 30 to 700 °C and heating rate of 10 °C min^{-1}.

2.3. Evaluation of photocatalytic activity

The photocatalytic activities of the as-synthesized samples were evaluated using the oxidation of two different contaminants, namely rhodamine B (RhB) and amiloride (AML), under visible irradiation. The chemical structures of the molecules are shown in Fig. 2. In a typical procedure, 10 mg of photocatalyst was placed in contact with 20 mL of an aqueous solution of RhB or AML (both at 10 mg L^{-1}). All the experiments were performed at 18 °C in a photoreactor equipped with six fluorescent lamps (Osram, 15 W, maximum intensity at 440 nm), under magnetic stirring. The representative image of the photoreactor is showed in Fig. S3. The photooxidation of RhB and AML was monitored at regular intervals at their maximum absorbances of 554 and 286 nm, respectively, using a Shimadzu UV-1601 PC spectrophotometer. Before starting the photocatalytic experiments, the suspensions were kept in the dark overnight in order to reach adsorption/desorption equilibrium between the contaminant and the photocatalyst surface. The adsorption capacity of both organic pollutants for all of the samples was negligible (<5%) after 12 h. The mechanism of oxidation of RhB dye promoted by the heterostructured 3CN:1Nb sample was investigated by adding the reactive species scavengers sodium oxalate (SO), tert-butanol (t-BuOH), and potassium bromate (KBrO$_3$) to the dye solution. These scavengers were chosen due to their capacities for trapping holes (h^+), hydroxyl radicals ($^\bullet$OH), and superoxide radicals ($O_2^{\bullet -}$), respectively [38–40].
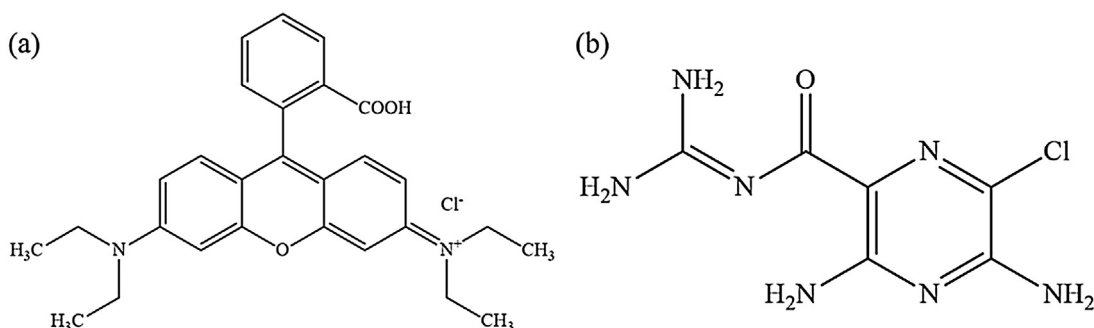
(a)

(b)

Fig. 2. Chemical structures of the (a) rhodamine B and (b) amiloride molecules.

3. Results and discussion

3.1. Characterization of the structural, electronic, and morphological properties of the materials

The XRD patterns of the as-synthesized g-C$_3$N$_4$, Nb$_2$O$_5$, and g-C$_3$N$_4$/Nb$_2$O$_5$ heterostructures are shown in Fig. S4. The pure g-C$_3$N$_4$ XRD pattern exhibited two main diffraction peaks at 27.3° (002) and 13.4° (100) assigned, respectively, to interplanar stacking of aromatic systems and interlayer structural packing of the tetragonal g-C$_3$N$_4$ phase (JCPDS 87-1526) [7]. The XRD pattern of pure Nb$_2$O$_5$ showed several large diffraction peaks that could be indexed as the orthorhombic Nb$_2$O$_5$ phase (JCPDS 28-0317) [23]. The XRD patterns of the g-C$_3$N$_4$/Nb$_2$O$_5$ heterostructures presented diffraction peaks corresponding to both g-C$_3$N$_4$ and Nb$_2$O$_5$ phases, indicating that the synthesis method employed did not change the crystalline structure of the catalysts. In addition, it was observed that an increase in the CN:Nb weight ratio caused a gradual decrease in the intensity of the characteristic g-C$_3$N$_4$ peaks, indicative of the incorporation of this phase in the heterostructured samples.

Fig. S5 shows the FTIR spectra for all the as-synthesized samples. The spectrum of pure g-C$_3$N$_4$ presented all the bands described in the literature [8,41], with intense bands at 812 cm^{-1}, 889 cm^{-1}, and in the range 1139–1689 cm^{-1} are assigned to out-of-plane bending vibration of heptazine rings, deformation mode of N—H bonds, and stretching modes of C—N heterocycles, respectively. A broad band at 3220 cm^{-1} corresponded to stretching vibrations of amino groups present at the end of the g-C$_3$N$_4$ structure. The spectrum of pure Nb$_2$O$_5$ exhibited a broad vibration band centered at about 3384 cm^{-1} attributed to the —OH stretching vibration of adsorbed water molecules on the surface of the oxide, while a broad band at 3231 cm^{-1} was due to the vibrational modes of the hydroxyl groups of Nb—OH [42,43]. The band at 1716 cm^{-1} and 1402 cm^{-1} are attributed to C=O and C(=O)$_2$ derived from the Nb precur-
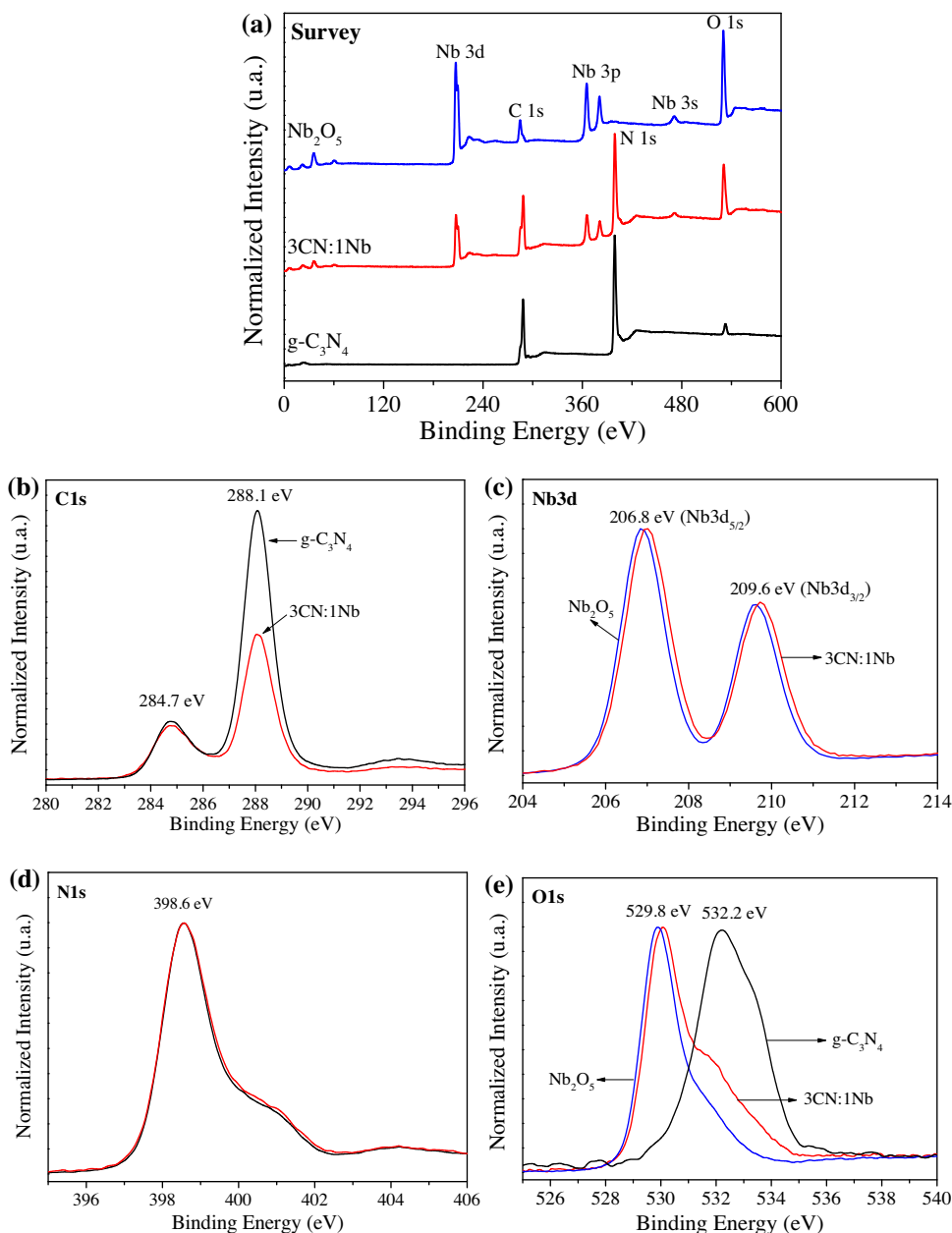

Fig. 3. XPS spectra of the as-synthesized g-C$_3$N$_4$, Nb$_2$O$_5$, and 3CN:1Nb heterostructure: (a) survey spectra, (b) high-resolution C 1s spectra, (c) high-resolution Nb 3d spectra, (d) high-resolution N 1s spectra, and (e) high-resolution O 1s spectra.
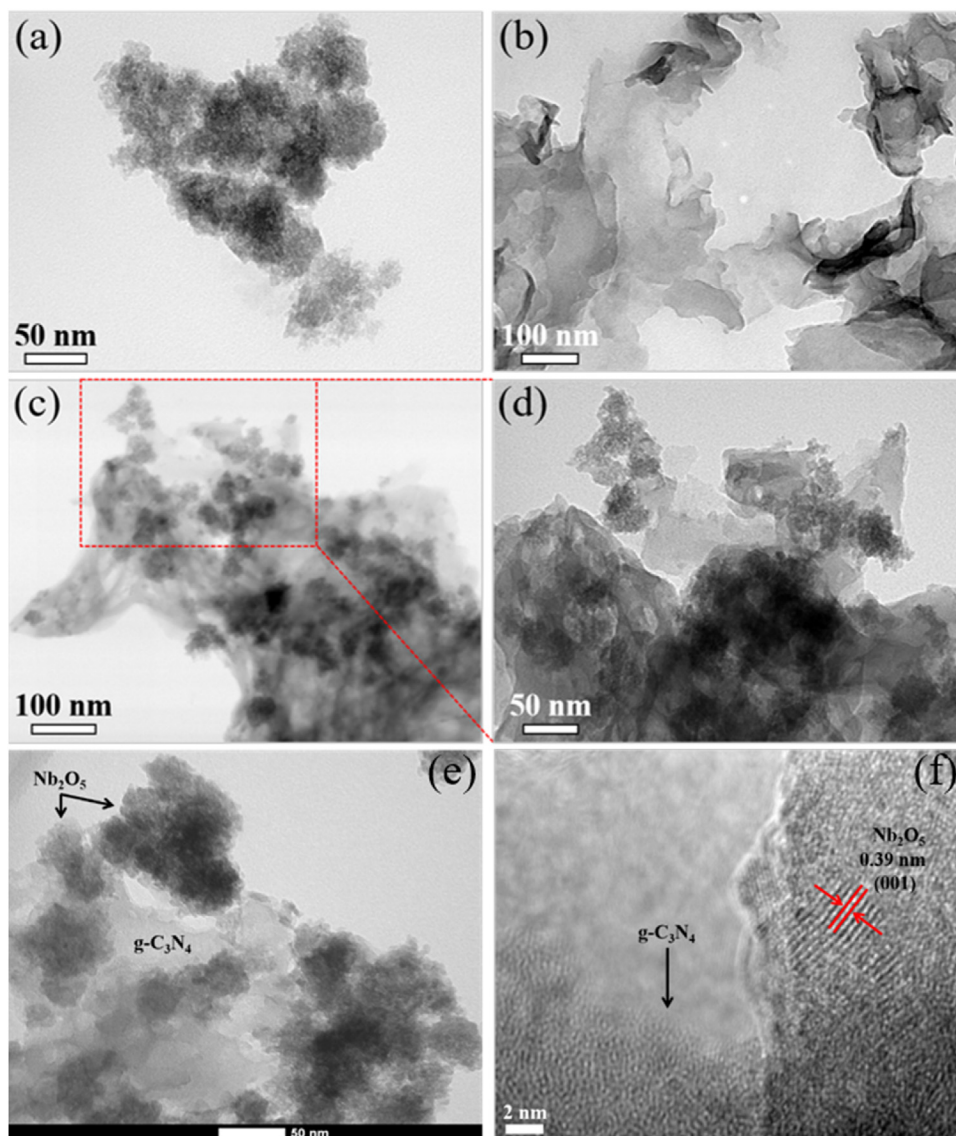
Fig. 4. TEM images of (a) Nb_2O_5 nanoparticles, (b) g-C_3N_4, and (c-f) 3CN:1Nb heterostructures.

sor [30]. A shoulder peak at 1101 cm^{-1} and an intense peak at 900 cm^{-1} were assigned to the stretching vibrations of Nb—O—C and Nb=O, respectively [42,44]. It can be seen that the FTIR spectra of the heterostructured samples exhibited characteristic peaks of both phases (g-C_3N_4 and Nb_2O_5), with few or negligible shifts. This could be explained by a relatively small quantity of interfaces available for interaction, compared to the bulk materials. An increase in the amount of Nb_2O_5 was accompanied by increases of the characteristic bands of this material.

XPS measurements were performed to confirm the surface composition and the chemical environment of Nb_2O_5, g-C_3N_4, and the 3CN:1Nb heterostructure. The results (survey and high-resolution spectra) are shown in Fig. 3. The survey XPS spectrum (Fig. 3a) of the 3CN:1Nb heterostructure exhibited strong C 1s and N 1s peaks related to the g-C_3N_4 phase, together with Nb 3d and O 1s peaks related to the Nb_2O_5 phase, without any contamination. The C 1s high-resolution spectra of g-C_3N_4 and the 3CN:1Nb heterostructure (Fig. 3b) showed two peaks centered at 284.7 and 288.1 eV. The peak at 284.7 eV corresponded to sp^2 C—C bonds of the carbon standard used to calibrate the binding energies. The peak located at 288.1 eV corresponded to N—C=N coordination present in the triazine rings of g-C_3N_4. As expected, the intensity of this peak was lower in the XPS spectrum for 3CN:1Nb, compared to the spectrum of pure g-C_3N_4. Deconvolution analysis of the N 1s spectra of g-C_3N_4 and the 3CN:1Nb heterostructure (Fig. S6) identified three peaks centered at 398.6, 399.7, and 400.8 eV, indicating the presence of N species with different chemical environments. These peaks could be assigned to N sp^2-bonded to C present in the triazine ring (C—N=C), tertiary nitrogen groups (N—$(C)_3$), and amino groups present at the end of the network (C—NH_3), respectively [35]. The Nb 3d high-resolution spectrum of pure Nb_2O_5 (Fig. 3c) exhibited two peaks at around 206.8 (Nb $3d_{5/2}$) and 209.6 eV (Nb $3d_{3/2}$). For the 3CN:1Nb heterostructure, the Nb $3d_{5/2}$ and Nb $3d_{3/2}$ peaks shifted to higher energies (Fig. 3c), compared to those of pure Nb_2O_5, evidencing the coordination between the atoms present on the Nb_2O_5 and g-C_3N_4 surfaces that resulted in the formation of effective heterojunctions between them. Deconvolution of the O 1s high-resolution spectrum of the 3CN:1Nb heterostructure (Fig. S6) resulted in two peaks centered at 530 and 531.5 eV, which were attributed to the Nb-O bond and oxygen in hydroxyl or oxalate groups derived from the precursor of niobium, respectively, in agreement with the FTIR observations [45]. In addition, the small peak of O 1s in g-C_3N_4 is assigned to adsorbed oxygen species.
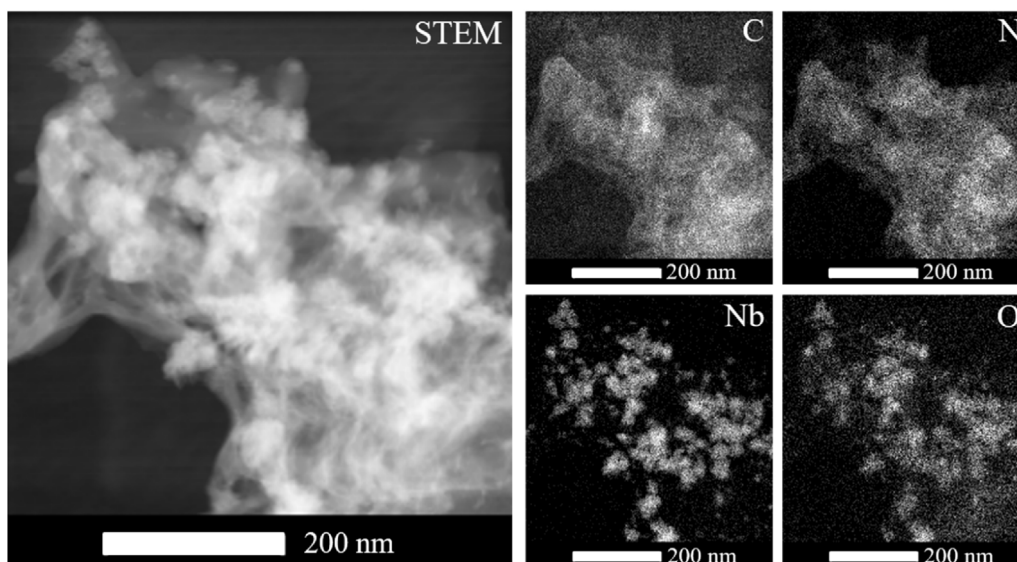
Fig. 5. STEM image and elemental distribution maps for C, N, Nb, and O of the 3CN:1Nb heterostructure.

SEM (Fig. S7) and TEM (Fig. 4) images were used to analyze the morphologies of the as-synthesized samples. The pure g-C$_3$N$_4$ and Nb$_2$O$_5$ samples exhibited laminar and spherical agglomerate morphologies, respectively (Fig. 4a and b), as reported elsewhere [7,23]. Additionally, it can be seen in Fig. 4c–e that the 3CN:1Nb heterostructure consisted of agglomerates of Nb$_2$O$_5$ nanoparticles quasi-homogeneously distributed on the laminar surface of g-C$_3$N$_4$. As shown in Fig. 4f, HRTEM image of the 3CN:1Nb sample showed an average inter-fringe distance of 0.39 nm, which could be attributed to the (001) plane of the orthorhombic Nb$_2$O$_5$ structure [46,47]. This finding confirmed the presence of Nb$_2$O$_5$ on the g-C$_3$N$_4$ surface, in agreement with the XRD observations (Fig. S4). Furthermore, elemental mapping analysis (Fig. 5) of the heterostructured 3CN:1Nb sample identified the presence of the elements C, N, Nb, and O sharing the same space, confirming that the agglomerates consisted of Nb$_2$O$_5$ nanoparticles in intimate contact with the g-C$_3$N$_4$ sheets. A notable feature was the satisfactory distribution of Nb$_2$O$_5$ over the g-C$_3$N$_4$ sheets, showing that the sonolysis procedure was highly effective in maximizing homogeneity, with the Nb$_2$O$_5$ particles being dispersed and showing similar sizes to those observed for the pristine material (Fig. 4a). The same features were observed in the SEM images of the 1CN:3Nb heterostructure (Fig. S7), which revealed Nb$_2$O$_5$ nanoparticles present on the g-C$_3$N$_4$ surface, showing that heterojunctions were formed using different CN:Nb weight ratios.

Diffuse reflectance spectroscopy measurements were carried out to evaluate the optical properties of the as-synthesized samples. The Tauc equation [48] was used to calculate the band gap energy values of g-C$_3$N$_4$, Nb$_2$O$_5$, and the g-C$_3$N$_4$/Nb$_2$O$_5$ heterostructures (Fig. 6). The band gap values of the pure g-C$_3$N$_4$ and Nb$_2$O$_5$ samples were approximately 2.8 and 3.2 eV, respectively, which were consistent with those described for these phases in the literature [23,49]. All the CN:Nb heterostructures (Fig. 6) showed band gap values similar to that obtained for g-C$_3$N$_4$, indicating that the optical properties of g-C$_3$N$_4$ were predominant in these heterostructures. Consequently, the CN:Nb heterostructures could be activated under visible irradiation, which is highly desirable for photocatalytic purposes.

The specific surface areas (SSA) of the g-C$_3$N$_4$, Nb$_2$O$_5$, and g-C$_3$N$_4$/Nb$_2$O$_5$ heterostructures samples were obtained by applying the BET model to the nitrogen adsorption data (Table 1). A higher specific surface area of g-C$_3$N$_4$ after the sonochemical treatment,
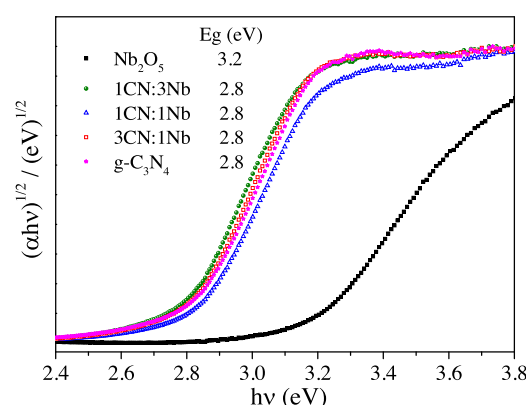

Fig. 6. Tauc plot obtained from UV–vis diffuse reflectance spectra data for Nb$_2$O$_5$, g-C$_3$N$_4$, and the g-C$_3$N$_4$/Nb$_2$O$_5$ heterostructures.

Table 1
Specific surface areas (SSAs) of as-synthesized samples.

Sample	SSA (m^2 g^{-1})		
	[a]After	[b]Calculated	[a]Before
Nb$_2$O$_5$	193.4	–	200.7
1CN:3Nb	133.9	155.2	–
1CN:1Nb	118.3	129.7	–
3CN:1Nb	113.4	104.2	–
g-C$_3$N$_4$	65.9	–	54.9

[a] Experimental data: after and before sonochemical treatment.
[b] Corresponds to the linear combination of the SSAs of the pristine materials according to the relative amount of each material.

compared to bulk g-C$_3$N$_4$, could be attributed to mechanical exfoliation of the sheets induced by the ultrasonic treatment [50]. On the other hand, the pure Nb$_2$O$_5$ sample did not show any significant change in specific surface area following the sonication process. The specific surface areas of the 3CN:1Nb, 1CN:1Nb, and 1CN:3Nb heterostructures were approximately 113.4, 118.3, and 156.2 m^2 g^{-1}, these values are very close to the expected ones for the linear combination of the SSAs of the g-C$_3$N$_4$ and Nb$_2$O$_5$ components.
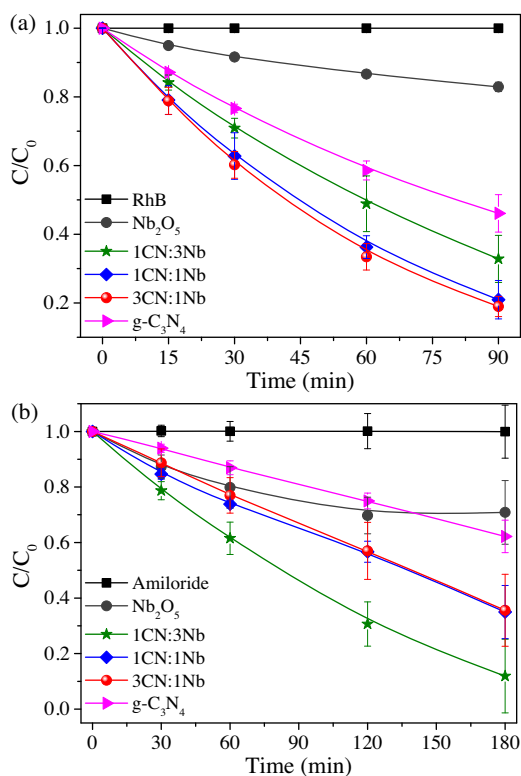
Fig. 7. Curves of (a) RhB dye and (b) drug AML photooxidation catalyzed by the as-synthesized samples under visible irradiation.

Table 2
Apparent rate constant (k_{app}) for the RhB dye and drug AML photocatalytic oxidation under different photocatalysts driven by visible radiation.

Photocatalysts	Rhodamine B		Amiloride	
	k_{app} x 10^3 (min^{-1})	R^2	k_{app} x 10^3 (min^{-1})	R^2
Nb_2O_5	2.6	0.96657	1.8	0.90727
g-C_3N_4	9.4	0.99919	3.1	0.99383
1CN:3Nb	11.4	0.99878	13.7	0.94184
1CN:1Nb	18.9	0.99828	6.6	0.96503
3CN:1Nb	20.2	0.99874	6.3	0.98337
3CN:1Nb-PM	13.2	0.98651	–	–
3CN:1Nb-H$_2$O	12.5	0.99732	–	–

ability of a sonochemical method based on surface charge-induced heteroaggregation for obtaining effective heterojunctions between two semiconductors. It was found that an increase in the CN:Nb weight ratio resulted in a significant increase in the photocatalytic activity of the heterostructure, indicating that the superior photocatalytic performance of the composite materials was probably due to interfacial charge transfer between the g-C_3N_4 and Nb_2O_5 semiconductors, which increased the lifetime of photogenerated electron/hole pairs.

Amiloride (AML) was used here to demonstrate the versatility of the as-synthesized samples to catalyze the oxidation of different kinds of organic pollutants. Fig. 7b shows the curves for AML photooxidation catalyzed by the as-synthesized photocatalysts under visible irradiation. As in the RhB photooxidation, no oxidation by direct photolysis was observed using an AML solution without any catalysts, under visible irradiation for 180 min. All the as-synthesized samples were photoactive for AML oxidation, since the kinetic curves decreased faster than the direct photolysis curve. The apparent kinetic rate constants (k_{app}) for AML photooxidation are exhibited in Table 2. All the composite materials showed higher photoactivity, compared to the pure phases. The Fig. S8 shows the UV–vis spectra of amiloride during the photocatalytic experiments in the presence of the heterostructure. In contrast to the behavior observed with RhB, the 1CN:3Nb heterostructure was the most active, with an apparent kinetic rate constants approximately 6.2 and 4.5 times higher than those obtained for the pure Nb_2O_5 and g-C_3N_4 samples, respectively. These results were probably related to the differences in surface acidity, considering that Nb_2O_5 is highly acid. The AML molecule possesses basic groups (as shown in Fig. 2) that were probably able to interact with the acid surface, hence improving the oxidation process. On the other hand, RhB is a zwitterionic molecule [5], so the net charge in solution was expected to be zero. Therefore, the dye was less influenced by the surface acidity, compared to AML. These findings demonstrate the versatility of this material, since it could be used in certain selective oxidation procedures, while adjustment of its composition could be employed to enhance its performance in the oxidation of different substrates. Additionally, photocatalytic experiments under UV irradiation were performed and a similar behavior was observed for photooxidation of the RhB dye and drug AML catalyzed by the as-synthesized samples, in which the heterostructured g-C_3N_4/Nb_2O_5 samples exhibited higher photocatalytic activity than the isolated phases (Fig. S9 and Table S1). These findings confirmed the formation of effective heterojunctions between g-C_3N_4 and Nb_2O_5, resulting in superior photocatalytic performance of the heterostructured samples.

In order to understand the dynamics of the electron/hole pair recombinations of the as-synthesized materials, their lifetimes were calculated for the pure g-C_3N_4 and the 3CN:1Nb heterostructure samples using time-resolved photoluminescence, with excitation at 409 nm and monitoring of the photoluminescence decay spectra at 535 nm. The measurement was not performed for the pure Nb_2O_5, because this material has a band gap
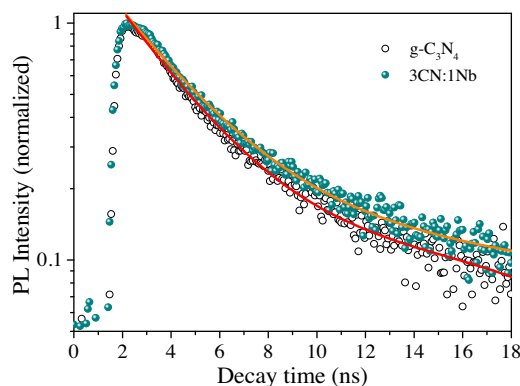
3.2. Evaluation of photocatalytic properties

The photocatalytic performances of the as-synthesized samples were evaluated using the oxidation of rhodamine B (RhB) dye under visible irradiation ($\lambda > 420$ nm). As shown in Fig. 7a, a blank test performed in the absence of the photocatalysts indicated that the contribution of direct photolysis was not significant and that adsorption was also negligible. Hence, a decrease in the RhB concentration could be attributed exclusively to its oxidation due to the effect of photocatalysis. The pure Nb_2O_5 sample exhibited low activity in RhB photooxidation, with an efficiency of 17% after 90 min under visible irradiation. This result was probably due to a photosensitization process [23], because this material exhibited an optical absorption edge at wavelengths lower than 387.5 nm ($\sim$3.2 eV), so it could only be directly activated under ultraviolet irradiation. The pure g-C_3N_4 sample showed RhB dye photooxidation efficiency of 54%, while the 1CN:3Nb, 1CN:1Nb, and 3CN:1Nb heterostructures exhibited efficiencies of approximately 67, 79, and 81%, respectively. Additionally, the 3CN:1Nb heterostructure showed higher photoactivity than the 3CN:1Nb-PM and 3CN:1Nb-H$_2$O samples, as shown in Fig. S2. Quantitative determination of the photocatalytic efficiencies of the different samples in RhB oxidation was achieved by calculating the kinetic rate constants of the reactions catalyzed by the materials. It was assumed that the reactions followed apparent first-order kinetics, described by the equation: $-\ln(C/C_0) = k_{app}t$, where C_0 and C are the initial RhB dye concentration and the concentration at time "t", respectively, and k_{app} is the apparent rate constant (min^{-1}). Table 2 shows the k_{app} values for all the as-synthesized samples. The value of k_{app} obtained for the 3CN:1Nb heterostructure was approximately 2.2 and 9.4 times higher than those obtained for pure g-C_3N_4 and Nb_2O_5, respectively. Additionally, the 3CN:1Nb heterostructure showed 1.5 and 1.6 times higher than those obtained for 3CN:1Nb-PM and 3CN:1Nb-H$_2$O samples (Table 2), respectively, indicating the suit-

Fig. 8. Time-resolved fluorescence decay spectra of g-C$_3$N$_4$ and the 3CN:1Nb heterostructure excited by laser irradiation at 409 nm and monitored at 535 nm. The solid lines are the results of the kinetic fits.

Table 3
Radiative fluorescence lifetimes of the photoexcited charge carriers in g-C$_3$N$_4$ and the 3CN:1Nb heterostructure.

Sample	τ_1 [ns]	τ_2 [ns]
g-C$_3$N$_4$	2.03	14.38
3CN:1Nb	2.21	14.64

of ~3.2 eV (Fig. 6) and is not activated by laser excitation at 409 nm. Fig. 8 shows a comparison of the time-resolved photoluminescence decay spectra of g-C$_3$N$_4$ and the 3CN:1Nb heterostructure. For both samples, the fluorescence decay was fitted using a bi-exponential decay function (Fig. 8). The values of the lifetime constants (τ) are shown in Table 3. Higher lifetime constants (τ_1 and τ_2) were obtained for the 3CN:1Nb heterostructure, compared to pure g-C$_3$N$_4$. These results confirm the formation of the type-II heterostructure, since this kind of heterostructure provides a spatial separation of the electron/hole pair driven by the difference between the reduction potentials of the g-C$_3$N$_4$ and Nb$_2$O$_5$ semiconductors, resulting in an increase in its lifetime [16,17]. As illustrated in Fig. S10, the photogenerated electrons in the conduction band of g-C$_3$N$_4$ (−1.23 eV), instead of returning quickly to its valence band, migrate to the conduction band of Nb$_2$O$_5$ (−0.80 eV), while the photogenerated holes in the valence band of Nb$_2$O$_5$ (+2.3 eV) migrate to the valence band of g-C$_3$N$_4$ (+1.40 eV) [22,51,52]. The increase in the lifetime of the photogenerated charges observed for the 3CN:1Nb heterostructure explains its higher photocatalytic performance in the oxidation of RhB and AML than that of the pristine g-C$_3$N$_4$, as shown in Fig. 7a and b. These findings demonstrated the formation of effective heterojunctions between the g-C$_3$N$_4$ and Nb$_2$O$_5$ phases, which favored the transfer of charge carriers between them and increased the lifetimes of the photogenerated charges.

3.3. Evaluation of photooxidation mechanism and stability

In order to understand the main mechanism of RhB and AML oxidation catalyzed by the g-C$_3$N$_4$/Nb$_2$O$_5$ heterostructures, evaluation was made of the effect of adding different reactive scavenger species directly to the 3CN:1Nb and 1CN:3Nb materials (Fig. 9). It was found that •OH radicals had no substantial influence on the oxidation profile, since oxidation tests with TBA showed almost the same result as the standard test, with oxidation of RhB occurring at a similar rate. On the other hand, the presence of sodium oxalate (hole scavenger) caused a large decrease in RhB photooxidation, showing that the photogenerated holes in the valence band played an important role in this process. The O$_2$•− radical made a minor contribution to RhB photooxidation, as can be observed
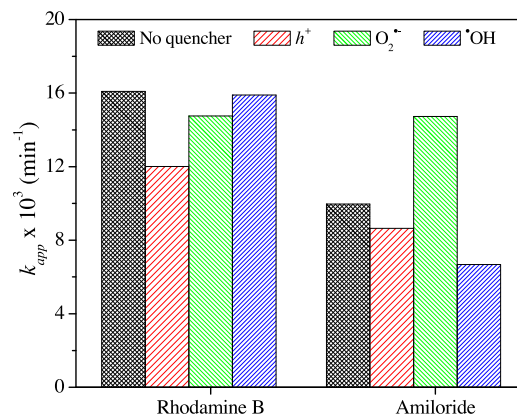

Fig. 9. Effects of different scavengers on RhB dye and drug AML photooxidation over the 3CN:1Nb and 1CN:3Nb heterostructures, respectively, under visible irradiation.
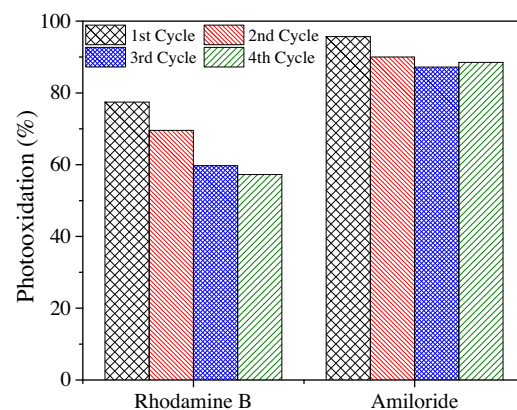

Fig. 10. Stability of the 3CN:1Nb and 1CN:3Nb heterostructures during consecutive cycles of RhB and AML photooxidation, respectively, under visible irradiation.

in Fig. 9, with the presence of KBrO$_3$ (electron scavenger) causing only a small decrease. These results indicated that the direct oxidation (i.e., hole attack) of the rhodamine B molecules was the most important mechanism, so the interaction between the substrate and the g-C$_3$N$_4$/Nb$_2$O$_5$ heterostructure surface was the first step of the oxidation mechanism.

Regarding the mechanism of the AML photooxidation, it was found that the presence of sodium oxalate (hole scavenger) caused only a small decrease in this process. On the other hand, the presence of KBrO$_3$ (electron scavenger) caused a significant increase in AML photooxidation. This result is most likely due to the increase in the lifetime of the photogenerated holes, leading to a higher •OH formation. In addition, it was observed a large decrease in the presence of TBA (•OH scavenger), showing that the indirect oxidation promoted by hydroxyl radical generation was the main mechanism for drug AML photooxidation process.

The stability of a photocatalyst is a crucial parameter in catalytic applications such as the treatment of wastewater. The stability of the 3CN:1Nb and 1CN:3Nb heterostructures, which were chosen due to their higher photoactivities (Fig. 7a and b), was evaluated during the photooxidation of RhB dye and the drug AML under visible irradiation. After each cycle of the photocatalytic reaction, the photocatalyst was recovered by centrifugation and transferred to a fresh pollutant solution to repeat the reaction under identical conditions. The results (Fig. 10) showed that the heterostructures exhibited good stability, since the photocatalytic efficiency decreased by only 23% and 7% to 3CN:1Nb and 1CN:3Nb, respectively, after four cycles of reuse. This decrease in photooxidation efficiency may be related to two factors: loss of material by leaching

during the reuse process or chances of physical-chemical properties such as morphology, surface groups, and structure. As shown in Fig. S11, the SEM, FTIR, and XRD characterizations were performed before and after the photocatalytic experiments and the properties of the materials remained practically unchanged, thus the leaching loss was considered to be the responsible for the loss of material activity.

4. Conclusions

In summary, g-C_3N_4/Nb_2O_5 heterostructures with different CN:Nb weight ratios were successfully obtained using an efficient and versatile method based on surface charge-induced heteroaggregation combined with a sonochemical treatment. The g-C_3N_4/Nb_2O_5 heterostructures exhibited higher photocatalytic activities towards the oxidation of RhB and AML under visible irradiation, compared to the pure g-C_3N_4 and Nb_2O_5 phases. The 3CN:1Nb and 1CN:3Nb heterostructures showed the highest photocatalytic performances in the oxidation of RhB and AML, respectively, because these substrates interacted differently with the heterostructure surfaces. The direct (i.e., hole attack) and indirect (i.e., •OH attack) mechanisms play the most important role in the oxidation of RhB and AML, respectively, catalyzed by the g-C_3N_4/Nb_2O_5 heterostructures. The enhancement of their photoactivities was attributed to longer lifetimes of the electron/hole pairs, due to the migration of photogenerated charge carriers between g-C_3N_4 and Nb_2O_5. In addition, it was demonstrated that the g-C_3N_4/Nb_2O_5 heterostructures exhibited satisfactory photostability, even after four successive reuse cycles.

Appendix A. Supplementary data

Supplementary data associated with this article can be found, in the online version, at http://dx.doi.org/10.1016/j.apcatb.2017.05.038.

References

[1] Y.N.B. Li, D.E. Moore, B.N. Tattam, Photodegradation of amiloride in aqueous solution, Int. J. Pharm. 183 (1999) 109–116, http://dx.doi.org/10.1016/S0378-5173(99)00035-6.

[2] P. Calza, C. Massolino, G. Monaco, C. Medana, C. Baiocchi, Study of the photolytic and photocatalytic transformation of amiloride in water, J. Pharm. Biomed. Anal. 48 (2008) 315–320, http://dx.doi.org/10.1016/j.jpba.2008.01.014.

[3] M.B. Ahmed, J.L. Zhou, H.H. Ngo, W. Guo, N.S. Thomaidis, J. Xu, Progress in the biological and chemical treatment technologies for emerging contaminant removal from wastewater: a critical review, J. Hazard. Mater. 323 (2016) 274–298, http://dx.doi.org/10.1016/j.jhazmat.2016.04.045.

[4] L. Lin, H. Wang, P. Xu, Immobilized TiO_2-reduced graphene oxide nanocomposites on optical fibers as high performance photocatalysts for degradation of pharmaceuticals, Chem. Eng. J. 310 (2017) 389–398, http://dx.doi.org/10.1016/j.cej.2016.04.024.

[5] V.R. de Mendonça, H.A.J.L. Mourão, A.R. Malagutti, C. Ribeiro, The role of the relative dye/photocatalyst concentration in TiO_2 assisted photodegradation process, Photochem. Photobiol. 90 (2014) 66–72, http://dx.doi.org/10.1111/php.12175.

[6] A. Thomas, A. Fischer, F. Goettmann, M. Antonietti, J.-O. Müller, R. Schlögl, J.M. Carlsson, Graphitic carbon nitride materials: variation of structure and morphology and their use as metal-free catalysts, J. Mater. Chem. 18 (2008) 4893, http://dx.doi.org/10.1039/b800274f.

[7] S. Martha, A. Nashim, K.M. Parida, Facile synthesis of highly active g-C_3N_4 for efficient hydrogen production under visible light, J. Mater. Chem. A 1 (2013) 7816, http://dx.doi.org/10.1039/c3ta10851a.

[8] X. Fan, Z. Xing, Z. Shu, L. Zhang, L. Wang, J. Shi, Improved photocatalytic activity of g-C_3N_4 derived from cyanamide–urea solution, RSC Adv. 5 (2015) 8323–8328, http://dx.doi.org/10.1039/C4RA16362A.

[9] S. Cao, J. Yu, g-C_3N_4-based photocatalysts for hydrogen generation, J. Phys. Chem. Lett. 5 (2014) 2101–2107.

[10] Z. Zhao, Y. Sun, F. Dong, F. Dong, Graphitic carbon nitride based nanocomposites: a review, Nanoscale 7 (2015) 15–37, http://dx.doi.org/10.1039/c4nr03008g.

[11] P. Niu, L. Zhang, G. Liu, H.M. Cheng, Graphene-like carbon nitride nanosheets for improved photocatalytic activities, Adv. Funct. Mater. 22 (2012) 4763–4770, http://dx.doi.org/10.1002/adfm.201200922.

[12] Z. Jin, Q. Zhang, S. Yuan, T. Ohno, Synthesis high specific surface area nanotube g-C_3N_4 with two-step condensation treatment of melamine to enhance photocatalysis, RSC Adv. Supplement (2012) 1–4.

[13] H. Xu, J. Yan, X. She, L. Xu, J. Xia, Y. Xu, Y. Song, L. Huang, H. Li, Graphene-analogue carbon nitride: novel exfoliation synthesis and its application in photocatalysis and photoelectrochemical selective detection of trace amount of Cu^{2+}, Nanoscale 6 (2014) 1406–1415, http://dx.doi.org/10.1039/c3nr04759h.

[14] G. Liu, P. Niu, C. Sun, S.C. Smith, Z. Chen, G.Q. (Max) Lu, H.-M. Cheng, Unique electronic structure induced high photoreactivity of sulfur-doped graphitic C_3N_4, J. Am. Chem. Soc. 132 (2010) 11642–11648, http://dx.doi.org/10.1021/ja103798k.

[15] S. Cao, J. Jiang, B. Zhu, J. Yu, Shape-dependent photocatalytic hydrogen evolution activity over a Pt nanoparticle coupled g-C_3N_4 photocatalyst, Phys. Chem. Chem. Phys. 18 (2016) 19457–19463, http://dx.doi.org/10.1039/C6CP02832B.

[16] Y. Wang, Q. Wang, X. Zhan, F. Wang, M. Safdar, J. He, Visible light driven type II heterostructures and their enhanced photocatalysis properties: a review, Nanoscale 5 (2013) 8326–8339, http://dx.doi.org/10.1039/c3nr01577g.

[17] W. Shi, N. Chopra, Nanoscale heterostructures for photoelectrochemical water splitting and photodegradation of pollutants, Nanomater. Energy 2 (2013) 158–178.

[18] X. Zhong, M. Jin, H. Dong, L. Liu, L. Wang, H. Yu, S. Leng, G. Zhuang, X. Li, J. Wang, TiO_2 nanobelts with a uniform coating of g-C_3N_4 as a highly effective heterostructure for enhanced photocatalytic activities, J. Solid State Chem. 220 (2014) 54–59, http://dx.doi.org/10.1016/j.jssc.2014.08.016.

[19] J. Tian, Q. Liu, A.M. Asiri, X. Sun, Y. He, Ultrathin graphitic C_3N_4 nanofibers: hydrolysis-driven top-down rapid synthesis and application as a novel fluorosensor for rapid, sensitive, and selective detection of Fe^{3+}, Sens. Actuators B Chem. 216 (2015) 453–460, http://dx.doi.org/10.1016/j.snb.2015.04.075.

[20] H. Yiming, Y. Wang, L. Zhang, B. Teng, M. Fan, High-efficiency conversion of CO_2 to fuel over ZnO/g-C_3N_4 photocatalyst, Appl. Catal. B Environ. 168 (2015) 1–8, http://dx.doi.org/10.1016/j.apcatb.2016.05.057.

[21] W. Wang, B. Huang, X. Liu, X. Qin, X. Zhang, Y. Dai, Hydrothermal synthesis of C_3N_4/$BiOIO_3$ heterostructures with enhanced photocatalytic properties, J. Colloid Interface Sci. 442 (2015) 97–102, http://dx.doi.org/10.1016/j.jcis.2014.11.061.

[22] S.M. Lam, J.C. Sin, I. Satoshi, A.Z. Abdullah, A.R. Mohamed, Enhanced sunlight photocatalytic performance over Nb_2O_5/ZnO nanorod composites and the mechanism study, Appl. Catal. A Gen. 471 (2014) 126–135, http://dx.doi.org/10.1016/j.apcata.2013.12.001.

[23] O.F. Lopes, E.C. Paris, C. Ribeiro, Synthesis of Nb_2O_5 nanoparticles through the oxidant peroxide method applied to organic pollutant photodegradation: a mechanistic study, Appl. Catal. B Environ. 144 (2014) 800–808, http://dx.doi.org/10.1016/j.apcatb.2013.08.031.

[24] O.F. Lopes, V.R. De Mendonça, F.B.F. Silva, E.C. Paris, C. Ribeiro, Niobium oxides an overview of the synthesis of Nb_2O_5 and its application in heterogeneous photocatalysis, Quim. Nova 38 (2014) 106–117, http://dx.doi.org/10.5935/0100-4042.20140280.

[25] T.A. Sedneva, E.P. Lokshin, M.L. Belikov, A.T. Belyaevskii, TiO_2- and Nb_2O_5-based photocatalytic composites, Inorg. Mater. 49 (2013) 382–389, http://dx.doi.org/10.1134/S0020168513040134.

[26] A.E. Nogueira, O.F. Lopes, A.B.S. Neto, C. Ribeiro, Enhanced Cr(VI) photoreduction in aqueous solution using Nb_2O_5/CuO heterostructures under UV and visible irradiation, Chem. Eng. J. 312 (2017) 220–227, http://dx.doi.org/10.1016/j.cej.2016.11.135.

[27] Z. Yue, D. Chu, H. Huang, J. Huang, P. Yang, Y. Du, M. Zhu, C. Lu, A novel heterogeneous hybrid by incorporation of Nb_2O_5 microspheres and reduced

graphene oxide for photocatalytic H 2 evolution under visible light irradiation, RSC Adv. 5 (2015) 47117–47124, http://dx.doi.org/10.1039/C5RA05348J.

[28] L.C.A. Oliveira, M. Gonçalves, M.C. Guerreiro, T.C. Ramalho, J.D. Fabris, M.C. Pereira, K. Sapag, A new catalyst material based on niobia/iron oxide composite on the oxidation of organic contaminants in water via heterogeneous Fenton mechanisms, Appl. Catal. A Gen. 316 (2007) 117–124, http://dx.doi.org/10.1016/j.apcata.2006.09.027.

[29] Y. Hong, C. Li, G. Zhang, Y. Meng, B. Yin, Y. Zhao, W. Shi, Efficient and stable Nb_2O_5 modified g-C_3N_4 photocatalyst for removal of antibiotic pollutant, Chem. Eng. J. 299 (2016) 74–84, http://dx.doi.org/10.1016/j.cej.2016.04.092.

[30] K.T.G. Carvalho, A.E. Nogueira, O.F. Lopes, G. Byzynski, C. Ribeiro, Synthesis of g-C_3N_4/Nb_2O_5 heterostructures and their application on removal of organic pollutants under visible and ultraviolet irradiation, Ceram. Int. 43 (2017) 3521–3530, http://dx.doi.org/10.1016/j.ceramint.2016.11.063.

[31] I. Khan, S. Ali, M. Mansha, A. Qurashi, Sonochemical assisted hydrothermal synthesis of pseudo-flower shaped Bismuth vanadate ($BiVO_4$) and their solar-driven water splitting application, Ultrason. Sonochem. 36 (2017) 386–392, http://dx.doi.org/10.1016/j.ultsonch.2016.12.014.

[32] J.H. Bang, K.S. Suslick, Applications of ultrasound to the synthesis of nanostructured materials, Adv. Mater. 22 (2010) 1039–1059, http://dx.doi.org/10.1002/adma.200904093.

[33] K. Okitsu, M. Ashokkumar, F. Grieser, Sonochemical synthesis of gold nanoparticles: effects of ultrasound frequency, J. Phys. Chem. B 109 (2005) 20673–20675, http://dx.doi.org/10.1021/jp0549374.

[34] N. Siedl, S.O. Baumann, M.J. Elser, O. Diwald, Particle networks from powder mixtures: generation of TiO_2-SnO_2 heterojunctions via surface charge-induced heteroaggregation, J. Phys. Chem. C 116 (2012) 22967–22973, http://dx.doi.org/10.1021/jp307737s.

[35] J. Liu, T. Zhang, Z. Wang, G. Dawson, W. Chen, Simple pyrolysis of urea into graphitic carbon nitride with recyclable adsorption and photocatalytic activity, J. Mater. Chem. 21 (2011) 14398, http://dx.doi.org/10.1039/c1jm12620b.

[36] I. Krivtsov, E.I. Garcia-Lopez, G. Marci, L. Palmisano, Z. Amghouz, J.R. Garcia, S. Ordonez, E. Diaz, Selective photocatalytic oxidation of 5-hydroxymethyl-2-furfural to 2, 5-furandicarboxyaldehyde in aqueous suspension of g-C_3N_4, Appl. Catal. B Environ. 204 (2017) 430–439, http://dx.doi.org/10.1016/j.apcatb.2016.11.049.

[37] B. Zhu, P. Xia, W. Ho, J. Yu, Isoelectric point and adsorption activity of porous g-C_3N_4, Appl. Surf. Sci. 344 (2015) 188–195, http://dx.doi.org/10.1016/j.apsusc.2015.03.086.

[38] R. Jin, W. Gao, J. Chen, H. Zeng, F. Zhang, Z. Liu, N. Guan, Photocatalytic reduction of nitrate ion drinking water by using metal-loaded $MgTiO_3$-TiO_2 composite semiconductor catalyst, J. Photochem. Photobiol. A Chem. 162 (2004) 585–590, http://dx.doi.org/10.1016/S1010-6030(03)00420-9.

[39] P. Liu, C. Li, Z. Zhao, G. Lu, H. Cui, W. Zhang, Induced effects of advanced oxidation processes, Sci. Rep. 4 (2014) 1–4, http://dx.doi.org/10.1038/srep04018.

[40] S.J. Armaković, S. Armaković, N.L. Finčur, F. Šibul, D. Vione, J.P. Šetrajčić, B.F. Abramović, Influence of electron acceptors on the kinetics of metoprolol photocatalytic degradation in TiO_2 suspension. A combined experimental and theoretical study, RSC Adv. 5 (2015) 54589–54604, http://dx.doi.org/10.1039/c5ra10523d.

[41] B. Zhu, P. Xia, Y. Li, W. Ho, J. Yu, Fabrication and photocatalytic activity enhanced mechanism of direct Z-scheme g-C_3N_4/Ag_2WO_4 photocatalyst, Appl. Surf. Sci. 391 (2017) 175–183, http://dx.doi.org/10.1016/j.apsusc.2016.07.104.

[42] M. Risctić, S. Popović, S. Musić, Sol-gel synthesis and characterization of Nb_2O_5 powders, Mater. Lett. 58 (2004) 2658–2663, http://dx.doi.org/10.1016/j.matlet.2004.03.041.

[43] A. Esteves, L.C.A. Oliveira, T.C. Ramalho, M. Goncalves, A.S. Anastacio, H.W.P. Carvalho, New materials based on modified synthetic Nb_2O_5 as photocatalyst for oxidation of organic contaminants, Catal. Commun. 10 (2008) 330–332, http://dx.doi.org/10.1016/j.catcom.2008.09.012.

[44] A.G.S. Prado, L.B. Bolzon, C.P. Pedroso, A.O. Moura, L.L. Costa, Nb_2O_5 as efficient and recyclable photocatalyst for indigo carmine degradation, Appl. Catal. B Environ. 82 (2008) 219–224, http://dx.doi.org/10.1016/j.apcatb.2008.01.024.

[45] X. Ma, Y. Chen, H. Li, X. Cui, Y. Lin, Annealing-free synthesis of carbonaceous Nb_2O_5 microspheres by flame thermal method and enhanced photocatalytic activity for hydrogen evolution, Mater. Res. Bull. 66 (2015) 51–58, http://dx.doi.org/10.1016/j.materresbull.2015.02.005.

[46] O.F. Lopes, E.C. Paris, C. Ribeiro, Synthesis of Nb_2O_5 nanoparticles through the oxidant peroxide method applied to organic pollutant photodegradation: a mechanistic study, Appl. Catal. B Environ. 144 (2014) 800–808, http://dx.doi.org/10.1016/j.apcatb.2013.08.031.

[47] J. Xue, R. Wang, Z. Zhang, S. Qiu, Facile preparation of C, N co-modified Nb_2O_5 nanoneedles with enhanced visible light photocatalytic activity, Dalt. Trans. 45 (2016) 16519–16525, http://dx.doi.org/10.1039/C6DT03548E.

[48] A.B. Murphy, Band-gap determination from diffuse reflectance measurements of semiconductor films, and application to photoelectrochemical water-splitting, Sol. Energy Mater. Sol. Cells 91 (2007) 1326–1337.

[49] W.-J. Ong, L.-L. Tan, Y.H. Ng, S.-T. Yong, S.-P. Chai, Graphitic carbon nitride (g-C_3N_4)-based photocatalysts for artificial photosynthesis and environmental remediation: are we a step closer to achieving sustainability? Chem. Rev. 116 (2016), http://dx.doi.org/10.1021/acs.chemrev.6b00075.

[50] S. Yang, Y. Gong, J. Zhang, L. Zhan, L. Ma, Z. Fang, R. Vajtai, X. Wang, P.M. Ajayan, Exfoliated graphitic carbon nitride nanosheets as efficient catalysts for hydrogen evolution under visible light, Adv. Mater. 25 (2013) 2452–2456, http://dx.doi.org/10.1002/adma.201204453.

[51] Y. Shiraishi, S. Kanazawa, Y. Kofuji, H. Sakamoto, S. Ichikawa, S. Tanaka, T. Hirai, Sunlight-driven hydrogen peroxide production from water and molecular oxygen by metal-free photocatalysts, Angew. Chem. Int. Ed. 53 (2014) 13454–13459, http://dx.doi.org/10.1002/anie.201407938.

[52] Y. Cui, Z. Ding, P. Liu, M. Antonietti, Metal-free activation of H_2O_2 by g-C_3N_4 under visible light irradiation for the degradation of organic pollutants, Phys. Chem. Chem. Phys. 14 (2012) 1455–1462, http://dx.doi.org/10.1039/c1cp22820j.